Joint falsification of gravity, magnetotelluric and surface-wave data resolves a fertile-corridor discriminator: the Al Amar suture, Arabian Shield

Jef Caers

Department of Earth and Planetary Sciences, Stanford University, Stanford, CA, USA

jcaers@stanford.edu

ORCID: https://orcid.org/0000-0003-0262-9905

This is a non-peer-reviewed preprint submitted to EarthArXiv.

The manuscript will shortly be submitted to *Geophysical Journal International* for peer review.

A companion paper, *A language model as a compiler: from tectonic narrative to a falsifiable prior*, is in preparation.

Draft v3, July 16, 2026

Joint falsification of gravity, magnetotelluric and surface-wave data resolves a fertile-corridor discriminator: the Al Amar suture, Arabian Shield

Jef Caers

Department of Earth and Planetary Sciences, Stanford University, Stanford, CA, USA

jcaers@stanford.edu

Draft v3 | Running title: *Joint falsification of a fertile-corridor discriminator*

Summary

A prospective mineral province is defined by deep structure. Sutures, shear zones, arc roots, and fluid corridors control where mineral systems form. Most of this structure is buried. It is known only from sparse geophysical data, and any one dataset permits several geological interpretations. This paper describes a prototype that converts a geologist's tectonic history into a falsifiable prior on deep petrophysical structure, and then asks which measurements separate geologically distinct histories.

A structural geologist writes the tectonic history in ordinary language. A language model compiles that text into typed, distributional, provenance-tagged constraints. The model transcribes constraints. It does not invent geology. The constraints drive a coarse lithospheric generator that produces three fields: density, shear-wave velocity, and electrical resistivity. Forward models compute the gravity, magnetic, surface-wave dispersion, and magnetotelluric response of those fields. Candidate scenarios are then tested by falsification. We ask whether each scenario's predicted data envelope is consistent with the observations. We do not seek the single best-fitting model.

We apply the method to the Al Amar–Halaban suture and the Najd fault system on the eastern Arabian Shield (Ar Rayn terrane). A fertile deep corridor changes crustal density by a small amount, lowers shear velocity by about 3 to 6 per cent, and raises deep (15 to 40 km) electrical conductance by a factor of about six. No single dataset separates this corridor from barren alternatives. We show this with an ablation in which each barren rival is built to match the fertile corridor on one dataset. Gravity and magnetics cannot reject a barren body of the same density and susceptibility. Dispersion cannot reject a barren body with the same velocity. Magnetotellurics rejects a resistive barren twin, so it is required. It cannot reject barren lower-crustal graphite, which reproduces the fertile conductance. Only the four datasets read together reject every rival. Every prior is tied to a public source. Every forward model is checked against an analytic limit. The falsification test is calibrated for its false-rejection rate. The modeled magnetic field is tested against a public satellite-airborne compilation over the corridor: each summary feature is individually admissible, and the joint test rejects an over-smooth source model. Adding the denser intrusive population the rejection calls for moves the observed data back inside the envelope, so the falsification loop closes on real magnetics. The same loop then runs on public gravity, seismic, and measured magnetotelluric data: each check either admits the model or rejects it for a nameable geological reason whose grounded correction admits it. The synthetic ablation and calibration run on grounded priors and synthetic truth. The quantities it cannot constrain from public data are the suture dip at depth, the three-dimensional velocity structure, the deep corridor conductivity, and the cover thickness. These are the measurements a targeted survey would supply.

Key words: Magnetotellurics; Gravity anomalies and Earth structure; Magnetic anomalies: modelling and interpretation; Surface waves and free oscillations; Inverse theory; Probability distributions.

1 Introduction

Mineral systems form along deep structure. At province scale, ore deposits are the small surface expressions of processes that operate through the whole lithosphere, and the features that control where they form, sutures, translithospheric shear zones, arc roots, and fluid corridors, are crustal-scale objects (McCuaig & Hronsky 2014). Most of this structure is buried. It is known only from sparse geophysical data, and any one dataset permits several geological interpretations. Exploration at this scale meets one problem again and again. Any single dataset fits many geological models, and the models that matter for prospectivity differ in ways that one dataset cannot separate.

This paper addresses greenfield exploration at country scale. The defining condition of greenfield work is that the major structures have not yet been found. The suture, the translithospheric shear, and the corridor where they intersect are not features to be refined. They are the targets. There is no mapped stratigraphy to deform, no drillhole to condition on, and no known architecture to fill in. What the region does have is a tectonic history: a structural geologist can state a defensible ordered sequence of subduction, arc growth, suturing, and later strike-slip faulting, and can state how well each part is known. At this stage the tectonic history is not one input among several. It is the leading prior. The question is which of a small set of candidate histories the region records, and which measurement would separate them.

The standard tool for interpreting a geophysical dataset is deterministic regularised inversion. The inversion minimises the data misfit together with a smoothness or minimum-structure norm and returns one model (Constable et al. 1987; deGroot-Hedlin & Constable 1990). Its three-dimensional potential-field form is the workhorse of exploration geophysics (Li & Oldenburg 1996, 1998). A geologist then interprets the recovered model. Joint inversion is the multi-dataset form of this approach, and the usual way to combine magnetotelluric, seismic, and potential-field data. Cross-gradient methods couple the datasets through a structural constraint and return one model that fits them together (Gallardo & Meju 2003), and three-dimensional frameworks extend the coupling to direct parameter relations (Moorkamp et al. 2011).

Geological knowledge enters this picture along two lines. The first is geological modelling. Kinematic modelling builds a three-dimensional structure by applying a sequence of deformation events, folding, shearing, intrusion, to an initial stratigraphy, and forward-models its potential fields (Jessell & Valenta 1996). Implicit structural modelling interpolates surfaces from mapped contacts and drillhole intersections, propagates uncertainty through ensembles of realisations, and increasingly connects to geophysical inversion (Jessell et al. 2014; Wellmann & Caumon 2018). Reviews of geological realism in inverse modelling make the case that the prior, not the regulariser, should carry the geology (Linde et al. 2015). The second line is probabilistic inversion and hypothesis testing. Monte Carlo methods sample the space of models consistent with prior and data (Mosegaard & Tarantola 1995). Tarantola (2006) argued that observations should be used to falsify candidate solutions rather than to select a best one. That argument has since been built into uncertainty-quantification protocols in which the prior itself is tested against data before any inference (Scheidt et al. 2018), and into the falsification of discrete geological hypotheses, such as competing ore-body shapes, against gravity and magnetic data at deposit scale (Wei et al. 2026).

Each line stops short of the greenfield problem, for a different reason. Regularised inversion works when the data constrain the model strongly, because the data term controls the result and the recovered features are required by the data. It fails in a specific way when the data are sparse or weakly informative, as they are for a deep target at reconnaissance scale. The regularisation term then controls the result, and the recovered model is close to the smoothest model the loose data allow. A geologist who interprets that model can read structure that the regularisation put there, and can miss a real body that the regularisation smoothed away. A narrow, high-contrast object is the hardest case, because a minimum-structure inversion penalises sharp contrasts and spreads a compact anomaly into a broad, weak one. The fertile corridor is exactly this kind of object: a narrow, deep conductor with a high resistivity contrast. Joint inversion inherits the same limit. It works when the data are dense enough to resolve a model. At the reconnaissance stage the data are sparse and the coverage is uneven, and a single resolved model would claim more than the data support.

The geological modelling line has a different limit: its scale. Kinematic and implicit models are built at deposit to camp scale, after the major structures have been discovered. A kinematic history in the style of Jessell & Valenta (1996) deforms a known starting stratigraphy, and an implicit model interpolates between mapped contacts and drillholes, so both presuppose the architecture and supply infill: the detail between observations of a structure whose existence and position are already established. Their priors refine geometry. In greenfield work the architecture is the hypothesis. The existence, position, and depth extent of the suture are the unknowns, and the prior that carries them is the tectonic history itself, stated in language, with the confidence of each statement carried in its wording. Today that narrative is translated into model parameters by hand. The translation is unrecorded, the width of each prior is not tied to the words that justified it, and no part of the chain from sentence to distribution can be audited or repeated. At reconnaissance scale, where the discrimination between histories is prior-dominated, this missing translation is the bottleneck.

Language models have begun to enter geoscience as domain assistants that generate answers (Deng et al. 2024; Lin et al. 2024) and as extractors of structured records from text (Dagdelen et al. 2024; Zhu et al. 2026). Neither produces what this gap needs, a distributional, executable, falsifiable prior. Here the model is restricted to transcription: it extracts the constraints the geologist's sentences license, and a deterministic rule turns each constraint into a maximum-entropy prior. The compilation method, its schema, and its validation are the subject of a companion paper (Caers in prep.); in this paper the compiled priors enter as expert-ratified, provenance-tagged inputs.

This paper contributes a controlled path from a written tectonic history to a falsifiable multiphysics prediction, and tests it. Three choices shape the method. First, the prior is compiled from the written history by a language model working as a constraint extractor, with a deterministic maximum-entropy rule turning each licensed constraint into the widest prior consistent with it, so vague wording produces a wide prior and every parameter keeps the clause and public source that licensed it. The compiler and its validation are developed in a companion paper (Caers in prep.); here the compiled priors are expert-ratified, auditable inputs. Second, the prior runs through a coarse lithospheric generator and explicit, benchmarked forward models, so the path from geology to data is open to inspection. Third, scenarios are judged by calibrated joint falsification in the tradition of Tarantola (2006) and Scheidt et al. (2018). We report which histories the data rule out. We do not report a single best-fit model, because at this scale a claim of resolution would be false. The coupling between datasets comes from the shared tectonic history, which predicts their joint behaviour, rather than from a cross-gradient term. The two approaches are complementary. Falsification screens hypotheses at the province scale. Joint inversion resolves structure once a target and dense data justify it.

We build and test the method on the eastern Arabian Shield: the Ar Rayn terrane, the Al Amar fault, and the Najd fault system. This is a Neoproterozoic continental-margin arc with gold, base-metal, porphyry-copper, and iron-oxide-copper-gold deposits (Doebrich et al. 2007). It carries an open question with direct economic weight. The Al Amar fault is read either as an intra-arc fault, with shallow arc-hosted deposits, or as an ophiolite-bearing suture, which can host deep fluid-focused corridors. The two readings differ in the deep structure the method is built to examine. Our main result is that the geophysical signature separating a fertile corridor from its barren alternatives appears only when the four datasets, gravity, magnetics, surface-wave dispersion, and magnetotellurics, are read together, tied through one tectonic history. Magnetotellurics is necessary, and because interconnected graphite mimics the fertile conductance, it is not sufficient on its own. The same calibrated test, applied to public aeromagnetic data over the corridor, rejects an over-smooth source model, and the denser intrusive population the rejection names then moves the data back inside the envelope, closing the falsification loop on real magnetics. The same loop repeats on public gravity, surface-wave, and measured magnetotelluric data, each within its stated scope.

The paper is organised as follows. Section 2 sets out the method: the tectonic event schema, the compiled priors of the Al Amar history with their provenance, the lithospheric generator and its grounded petrophysical priors, the benchmarked forward models, and the falsification test with its calibration; the compiler itself and its validation are the companion paper (Caers in prep.).

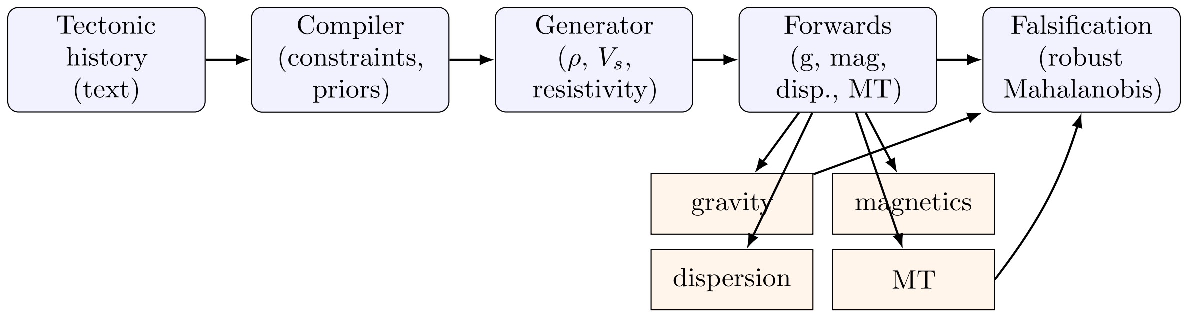

Figure 1: The five-stage pipeline. A tectonic history is compiled into a provenance-tagged prior, a coarse generator turns the prior into petrophysical fields, three forward models produce the four datasets, and candidate scenarios are tested by robust-Mahalanobis falsification.

Section 3 describes the Al Amar–Halaban and Najd case study and the prior corrections that compiling its history forced. Section 4 reports the results: the joint discriminator and the dataset ablation, the calibration of the test, and the consistency check against public aeromagnetic data. Section 5 discusses what the method fixes and what it leaves open, and Section 6 states the conclusions and the survey the unconstrained quantities recommend.

2 Methods

2.1 Overview

The method is a chain of five stages (Fig. 1). A structural geologist writes a tectonic history in ordinary language. A compiler turns the history into a set of typed, distributional, provenance-tagged tectonic events. A coarse lithospheric generator executes the events into three-dimensional fields of density, shear velocity, and electrical resistivity. It carries the magnetic susceptibility and Vp/Vs priors of each unit alongside, which the magnetic and dispersion forwards read. Forward models map the fields to gravity, magnetic, surface-wave dispersion, and magnetotelluric response. A robust-Mahalanobis test then falsifies candidate scenarios against data. The resolution at every stage is the resolution of country-scale reconnaissance. The contribution of this paper is the first stage, the translation from a tectonic history to a prior, and the test of that translation. The rest of the chain is standard geophysics. It is included so the prior can be pushed to observables and checked.

2.2 The tectonic event schema

The compiler emits instances of a fixed schema. The schema is a small set of tectonic event types with typed parameters. The types cover the events that build and modify a terrane at this scale: arc magmatism, ophiolite emplacement and suturing, transcurrent faulting, metasomatism, and cover deposition. Each event carries geometric parameters (strike, dip, offset, belt width, depth extent), a timing, and the petrophysical consequences it implies for density, magnetic susceptibility, resistivity, and seismic velocity. Every parameter is a distribution. None is a single value. Every parameter carries a provenance tag, which is the clause of the history that licensed it and the public source behind that clause. The schema is fixed and authored by hand.

It defines what the compiler is allowed to say. Each event type maps to a defined operation on the lithospheric model in the generator, so the schema is executable. Figure 21 shows five primitives of the schema, from the statement a geologist writes to the prior the compiler emits to the signature the forwards produce.

2.3 From history to prior

The written history is compiled into the typed events of the schema by a language model restricted to constraint extraction, clause by clause, with a deterministic maximum-entropy rule mapping each constraint to a distribution family and width, and a provenance tag tying every parameter to the clause and public source that licensed it. Statements that name a feature without constraining it leave the prior untouched, and assertions of ignorance widen it. The compiler, its prompt and schema, the single-author validation protocol with its objective over-extraction and monotonicity batteries, and the annotation-sensitivity analysis are the subject of the companion paper (Caers in prep.). For this paper the operative facts are two: every prior in Tables 1 and 2 was ratified by the author against its source before use, and six draft values were corrected during that ratification (Section 3), which is the audit trail working as intended.

2.4 Priors for the Al Amar history

Table 1 lists the structural random variables the history compiles to, each with its unit, its prior distribution, and its source. Most geometric parameters carry a draft prior, because public data do not yet constrain them, and these are among the quantities a survey would measure. The belt width, the sinistral Najd offset, and the Moho depth are grounded to public sources. Table 2 lists the petrophysical priors, one row per lithological unit. The serpentinised suture is the load-bearing case. Its density prior falls and its susceptibility prior rises together along the serpentinisation degree, so the belt reads as a magnetic and conductive body with a weak or negative gravity signature.

The generator then executes the compiled events into a coarse voxel volume. It builds the suture as a steep north-south surface at the compiled position and dip, waved along strike, and it shifts that surface across the Najd shear by the compiled sinistral offset. It fills the two arc terranes on either side, inserts the ophiolite belt at the compiled width, cuts the Najd shear zone, laps the cover in from the east, and, in the fertile scenario, places the deep corridor along the suture with an enhancement where the Najd crosses it. Each voxel then takes the petrophysical prior of its unit. The output is the density, shear-velocity, and resistivity field the forwards read, with the susceptibility and Vp/Vs priors carried alongside for the magnetic and dispersion forwards.

Figure 2 shows three draws of the same history. The tectonic order is fixed, so every sample has the two terranes, the suture between them, the Najd overprint, and the Moho. The geometry varies with the compiled priors: the suture position, its dip, the sinistral offset, the corridor extent, the Moho depth, and the cover thickness. Two draws carry a fertile corridor and one is

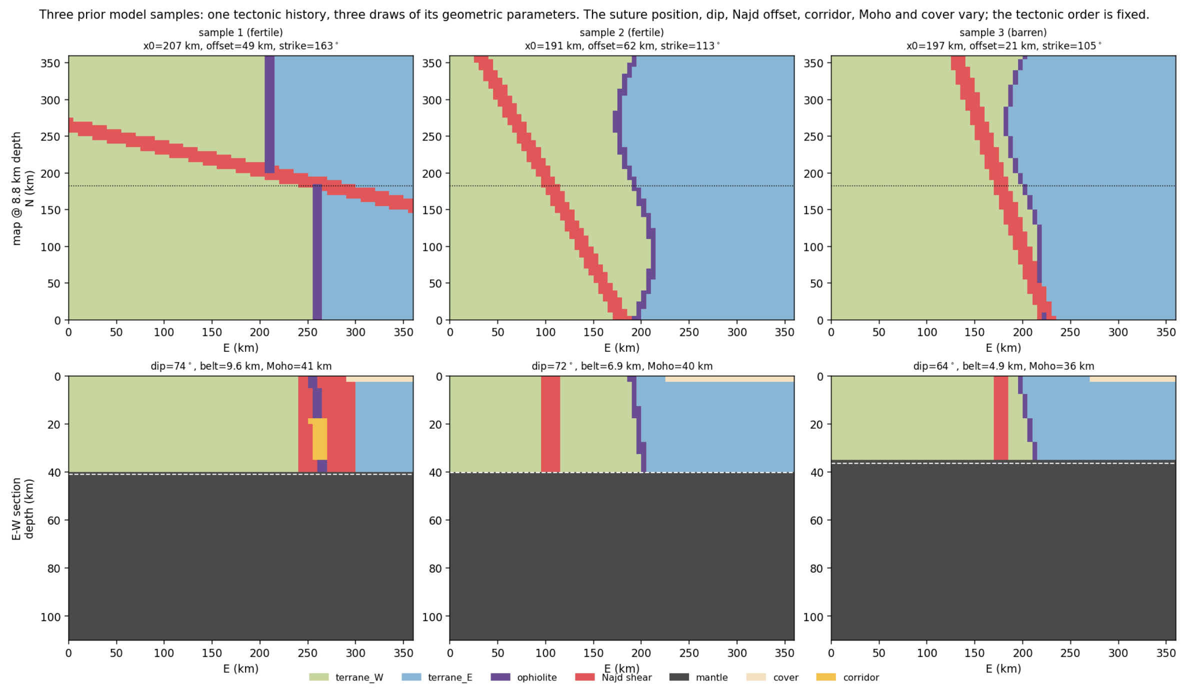

Figure 2: Three prior model samples. Each column is one draw of the geometric event parameters of the Al Amar history, executed by the generator. The top row is a map at 7.5 km depth; the bottom row is an east–west section through the box centre, with the Moho dashed. The suture position, dip, Najd offset and strike, corridor extent, Moho depth and cover all vary with their priors, while the tectonic order and the unit petrophysics are held fixed. Samples 1 and 2 carry a fertile corridor; sample 3 is barren.

barren, from the scenario variable. The prior-predictive spread at this scale is geometric, so the unit petrophysics sit at their central values while the structure moves. This is the ensemble the falsification test draws from.

2.5 Lithospheric generator and petrophysical priors

The generator executes the compiled events into a coarse three-dimensional model. Each unit carries priors on density, magnetic susceptibility, resistivity, shear velocity, and Vp/Vs. All priors are held in one module in which every value traces to a public reference. Densities come from whole-rock chemistry (Doebrich et al. 2007, Appendix A) through a silica-density relation and a rock-physics compilation (Hunt et al. 1995). Susceptibilities are bimodal: a paramagnetic floor from whole-rock iron content, and a ferromagnetic magnetite-series mode from rock-magnetic compilations (Clark 1997; Hunt et al. 1995). The two modes are kept separate because whole-rock chemistry cannot tell magnetite-series from ilmenite-series rocks apart. For the serpentinised suture the density and susceptibility priors are anti-correlated through the serpentinisation degree: density falls from about 3000 to about 2550 $\mathrm{kg\,m^{-3}}$ while susceptibility rises from about 10^{-3} to about 0.6 SI (Clark 1997). Resistivities follow the nearest magnetotelluric study on the shield (Bedrosian et al. 2019), which sets the lower-crustal background conductance (500 to 1500 S over 15 to 40 km) and identifies interconnected graphite as the mechanism that mimics a fertile corridor. The Vp/Vs ratio is 1.75 ± 0.07 from receiver functions (Blanchette et al. 2023), and agrees with the 1978 deep refraction profile (upper crust near 6.3, lower crust near 7.0,

Table 1: Structural random variables compiled from the Al Amar history. TN is a truncated normal $\mathrm{TN}(\mu, \sigma; [\ell, u])$, LN a log-normal with the stated median truncated to $[\ell, u]$, U a uniform, VM a von Mises with concentration κ, and Cat a categorical. Draft priors are first estimates awaiting a direct constraint. AHS26 is Al-Husseini & Stewart (2026); RF/ANT is the receiver-function and ambient-noise constraint (Blanchette et al. 2023).

Random variable	Unit	Prior	Source
Suture (Al Amar–Halaban)			
x_0: east–west position	km	TN(180, 30; [120, 240])	draft
δ: dip	deg	TN(72, 8; [55, 88])	draft
w: ophiolite belt width	km	LN(7; [2, 14])	AHS26 p.40
a_y: along-strike undulation	km	U(0, 25)	geometric
Amar orogeny			
t: crustal thickening	factor	U(1.0, 1.4)	orogeny
v: thrust vergence	deg	VM(90, κ=6)	draft
Najd shear			
ϕ: strike	deg	VM(130, κ=10)	Najd lit.
s_0: position across box	fraction	U(0.35, 0.65)	geometric
w_N: shear-zone width	km	LN(18; [6, 50])	draft
s: sinistral offset	km	TN(45, 22; [6, 80])	AHS26
Fertile corridor (metasomatism)			
z_t: top depth	km	TN(15, 5; [8, 28])	draft
z_b: base depth	km	TN(35, 6; [25, 55])	draft
h: half-width	km	LN(12; [4, 35])	draft
g: Najd enhancement	factor	U(1.5, 3.0)	model
Cratonisation and cover			
z_M: Moho depth	km	TN(38, 4; [30, 48])	RF/ANT
z_c: cover thickness	km	TN(1.2, 0.8; [0, 4])	draft
x_c: cover onlap	fraction	U(0.55, 0.80)	geometric
Scenario			
fertility	class	Cat(fertile 0.6, barren 0.4)	the ore question

mantle near 8.1 $\mathrm{km\,s^{-1}}$) (Mooney et al. 1985; Gettings et al. 1986). The ambient field is the IGRF value at the corridor (declination +3.20°, inclination +37.1°, intensity 42 773 nT), checked against an independent calculator. Remanent magnetisation is carried as a Koenigsberger-ratio magnitude prior with a uniform, marginalised direction, because no reliable Neoproterozoic pole exists for the terrane and later Najd rotation with greenschist remagnetisation would scramble any acquired direction.

2.6 Forward models

Three forward models map the fields to data. Each is self-contained and checked against an analytic or community limit. Mature community codes remain available for full three-dimensional work.

The gravity and magnetic forward is exact rectangular-prism summation with induced and remanent magnetisation; it reproduces the point-mass and dipole limits and the Laplace identity to machine precision. On a serpentinised suture the density falls and the susceptibility rises, so the body reads as a magnetic high with a weak or negative gravity signature. The dispersion

Table 2: Petrophysical priors, one row per lithological unit, from the grounded prior module. Density, V_s, and V_p/V_s are truncated normals; susceptibility χ and resistivity ρ_e are log-normals. The bracketed pair is the $\pm 2\sigma$ range. Sources: D, Doebrich et al. (2007) Appendix A chemistry; C, Clark (1997); H, Hunt et al. (1995); B, Bedrosian et al. (2019); RF, Blanchette et al. (2023). The ophiolite is the serpentinisation ladder: density falls as susceptibility rises.

Unit	ρ ($\mathrm{kg\,m^{-3}}$)	χ (SI)	ρ_e ($\Omega\,\mathrm{m}$)	V_s ($\mathrm{km\,s^{-1}}$)	V_p/V_s	Src
Arc crust W	2600–2820	10^{-4}–3×10^{-2}	10^{3}–10^{4}	3.4–3.7	1.70–1.78	D,C,H
Arc crust E	2620–2840	1.5×10^{-4}–5×10^{-2}	10^{3}–10^{4}	3.5–3.8	1.72–1.79	D,C
Alkali granite	2550–2680	6×10^{-5}–10^{-2}	2×10^{3}–10^{4}	3.5–3.7	1.68–1.74	D,C
Gabbro (mafic)	2880–3070	10^{-3}–9×10^{-2}	3×10^{2}–3×10^{3}	3.8–4.1	1.76–1.84	H,C
Ophiolite/suture	2550–3000	10^{-3}–6×10^{-1}	10^{0}–10^{3}	3.3–4.0	1.78–1.92	C,H
Mantle	3300–3350	10^{-4}–10^{-3}	10^{2}–5×10^{2}	4.4–4.7	1.76–1.82	B,RF
Asthenosphere	3280–3330	10^{-4}–10^{-3}	1.5×10^{1}–3×10^{1}	4.2–4.5	1.80–1.86	B
Fertile corridor	2900–3050	10^{-2}–3×10^{-1}	10^{0}–10^{1}	3.6–3.9	1.76–1.86	B,C
IOCG magnetite	3200–4500	10^{0}–10^{1}	10^{0}–10^{2}	3.8–4.2	1.80–1.88	D,H

forward is a propagator-matrix method checked against the analytic half-space Rayleigh limit; a 6 per cent deep velocity reduction in the corridor shifts phase velocity by about 3 per cent near 17 s, a weak and non-unique signal. The magnetotelluric forward is an exact one-dimensional recursion and a two-dimensional transverse-electric finite-difference solver that reproduces the one-dimensional limit and the COMMEMI 2D-1 community benchmark (Zhdanov et al. 1997); two dimensions are needed because the corridor is a laterally confined conductor, and a confined fertile corridor produces a localised 85 per cent deep apparent-resistivity drop, raising deep conductance from about 500 to about 3100 S. The solver is TE-mode; TM and anisotropic modelling, which bear on the graphite confounder, are the next step. The benchmark figures and full verification detail are in Appendix A.

2.7 Falsification and calibration

We falsify. We do not invert. For each scenario we draw a prior-predictive ensemble of petrophysical models, run each through the forwards, and reduce it to a feature vector of the diagnostic observables: gravity, magnetics, dispersion, and MT conductance. A dataset falsifies a scenario when the observed data fall outside the scenario's robust-Mahalanobis envelope. The envelope centre and covariance are robust estimates from the ensemble. The threshold is a high percentile of the ensemble's own robust-Mahalanobis distances, computed on a held-out calibration set. We do not use a chi-square quantile, because the features are non-Gaussian, mainly because the marginalised remanence direction gives the magnetic feature a wide, skewed spread, and a chi-square threshold is then miscalibrated. We calibrate the test by measuring the rate at which it rejects the true scenario as a function of ensemble size and feature dimensionality (Appendix B, Fig. 19). The false-rejection rate reaches its nominal value for ensembles of at least about fifty draws per dimension, and the chi-square threshold does not reach the nominal value even for large ensembles.

3 Case study: Al Amar–Halaban and Najd, Ar Rayn terrane

The Ar Rayn terrane is a Neoproterozoic continental-margin arc on the eastern Arabian Shield. The Al Amar fault bounds it on the west against the Ad Dawadimi terrane. Phanerozoic cover overlaps it on the east (Doebrich et al. 2007). It coincides with the north-trending central Arabian magnetic anomaly. The northwest-trending, sinistral Najd fault system cuts across it (the Ar-Rika–Qazaz shear zone, about 640 to 610 Ma). Its deposits, which include epithermal Au-Ag-Zn-Cu, orogenic Au, porphyry Cu, and magnetite-bearing iron-oxide-copper-gold, mark an oxidised, magnetite-series arc.

The question that controls prospectivity is the nature of the Al Amar fault. It is read either as an intra-arc structure with shallow arc-hosted systems (Doebrich et al. 2007), or as an ophiolite-bearing suture that can host deep fluid-focused corridors. The two readings differ in the deep structure the method examines.

The Al Amar history was compiled from two public sources: the terrane geology and metallogeny (Doebrich et al. 2007), and an aeromagnetic geodynamic reconstruction of the Najd system (Al-Husseini & Stewart 2026). Every prior parameter maps to a citation. Compiling the history forced six corrections to the initial draft priors. Najd offsets are sinistral only, not symmetric. The ophiolite belt is 2 to 12 km wide, which is distinct from the wider fault zone. The arc crust is lighter than first drafted, from the felsic-to-intermediate chemistry in the appendix. The Moho prior matches receiver-function depths near 38 km at the eastern shield boundary. A seventh correction, forced by the analogue MT study, carries the result. The diagnostic suture signature is magnetic and conductive. It is not a reliable gravity high. Lower-crustal conductivity is ambiguous between fertile mineralisation and barren interconnected graphite (Bedrosian et al. 2019).

4 Results

4.1 The joint discriminator

The main experiment is an ablation (Fig. 3). We set a fertile corridor as the truth. We then test whether each barren rival can be falsified using each subset of the four datasets. To make the test hard, each rival is built to match the fertile corridor on one dataset. A barren-resistive twin matches the fertile corridor on gravity, magnetics, and dispersion, and differs only in MT. A graphite scenario matches it on MT and differs on the other three. A dense-magnetic scenario matches it on gravity and magnetics. An intra-arc scenario matches it on dispersion. Features are generated end-to-end through the real forward models.

The outcome is clear. Every single dataset leaves at least one rival un-falsified, because each rival matches the fertile corridor on the dataset it was built to mimic. MT is required. Only MT falsifies the resistive twin, so no subset without MT works, and the gravity, magnetics, and dispersion trio fails on the twin at the nominal false-rejection rate. MT is also not enough on its own. It fails on the graphite scenario, because interconnected lower-crustal graphite reproduces the fertile conductance. This is the confounder identified in the analogue study, now quantified.

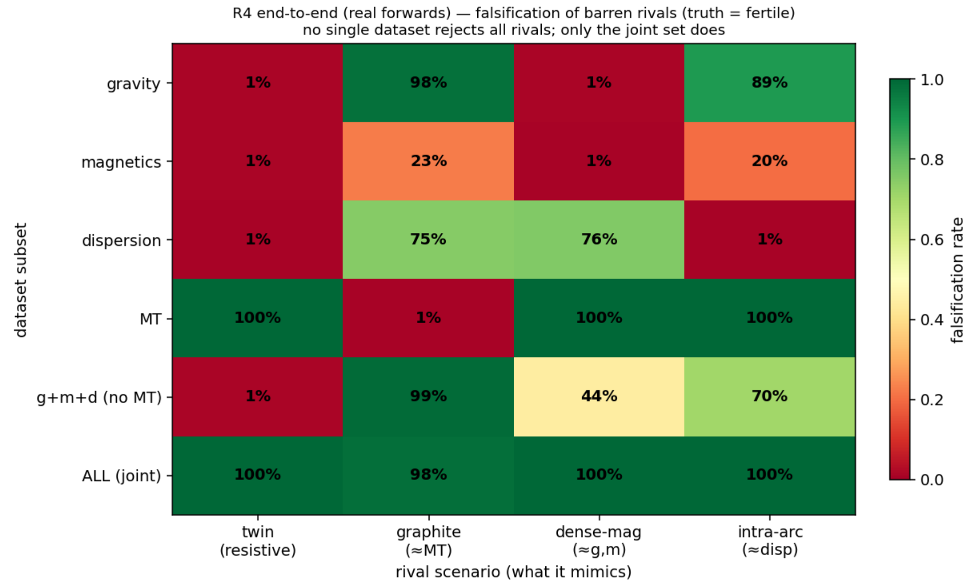

Figure 3: Falsification of the barren rivals with the truth set to fertile, features generated end-to-end through the real forwards. Green is a rival correctly rejected; red is a rival that survives. No single dataset rejects all rivals. MT alone fails on the graphite rival; the no-MT trio fails on the resistive twin; only the joint set rejects every rival.

All four datasets read together falsify every rival. The signature is joint, and the tie carries it, because the tectonic history predicts the joint behaviour of the four datasets. The end-to-end version adds one result. Magnetics is a weaker discriminator than a simpler treatment suggests, because the marginalised remanence direction makes the magnetic response ambiguous. This adds weight to the finding that MT and the tectonic tie do the work.

Table 4 (Appendix C) lists the feature priors of the five scenarios, in the same form as the structural and petrophysical tables. The fertile priors come from the grounded module (Table 2). Each rival keeps the fertile prior on the feature it mimics and takes a barren prior on the rest, which is the stated construction rule of the ablation.

Figure 4 is the prior-predictive check that precedes the test. For each physics it shows fifty forward-modelled samples from every scenario, three fertile samples drawn bold, and the observed data, here one realisation of the synthetic fertile truth. The figure shows the ablation's construction directly. In the gravity and magnetic panels the twin and dense-magnetic envelopes lie on top of the fertile one. In the dispersion panel the twin and intra-arc envelopes do. In the MT panel the graphite envelope does, and the twin, dense, and intra-arc envelopes separate cleanly. The observed sounding falls inside the fertile and graphite MT envelopes and outside the others.

Figures 5 and 6 show the test itself. The individual panels apply the robust-Mahalanobis test one dataset at a time. Each violin is the distribution of the observed ensemble's RMD under one scenario's envelope, divided by that scenario's held-out 99 per cent threshold, so values above one are falsified. Every rival survives the dataset it mimics, at the nominal rate near 1 per cent. The joint panel applies the test to all four datasets together. The observed ensemble sits inside the fertile envelope at the nominal rate and beyond every rival's threshold, at 98 per cent for graphite and 100 per cent for the rest. These plots are the graphical form of the rates in Fig. 3.

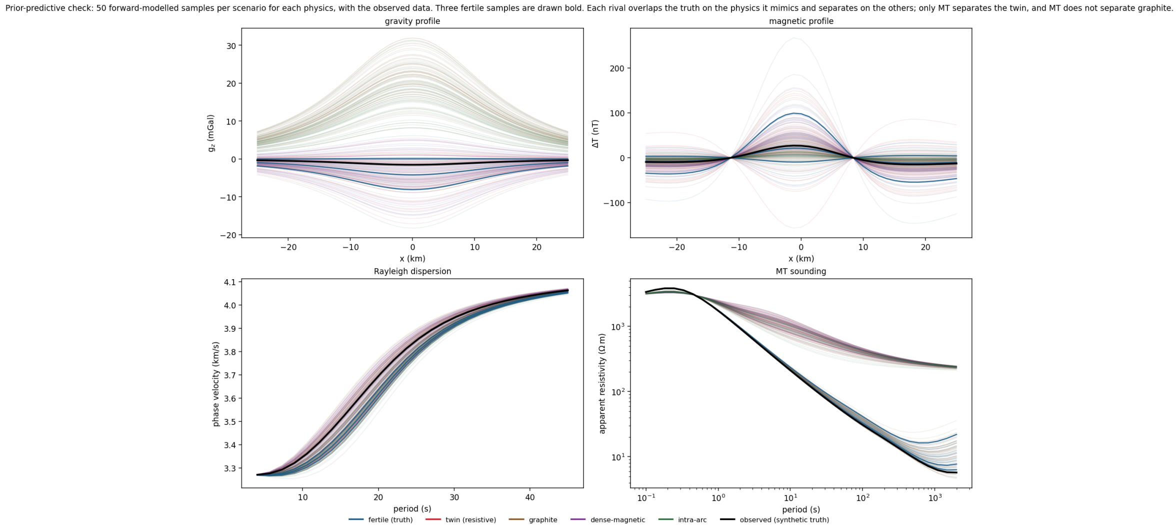

Figure 4: Prior-predictive check for the synthetic case. Each panel shows fifty forward-modelled samples per scenario for one physics (colours as in the legend), three fertile prior samples in bold, and the observed data, one realisation of the synthetic fertile truth (black). Each rival overlaps the truth on the physics it was built to mimic and separates on the others. Only MT separates the resistive twin, and MT does not separate graphite.

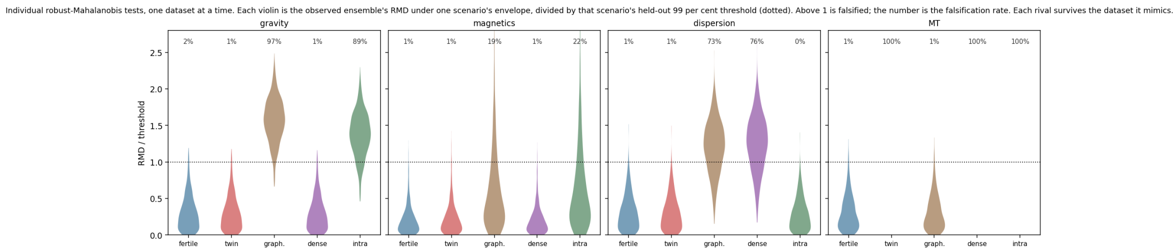

Figure 5: Individual robust-Mahalanobis tests, one dataset at a time. Each violin is the observed ensemble's RMD under one scenario's envelope, divided by that scenario's held-out 99 per cent threshold (dotted line). Values above one are falsified; the number over each violin is the falsification rate. Each rival survives the dataset it was built to mimic.

4.2 Robustness to out-of-model truth

The ablation tests each scenario against synthetic data drawn from the fertile prior. That is partly self-consistent: the observed data are a draw from the same distribution whose envelope admits them. To separate the discriminator from the way the truth is generated, we repeat the test with observed data from an independently constructed fertile lithosphere that is not a draw from any scenario prior. The corridor parameters are drawn from different distributions than the fertile prior; the four datasets carry feature-level contributions from structure the scenario forwards do not represent, a shallow intrusion in gravity and magnetics, a second deep conductor in magnetotellurics, and lateral velocity heterogeneity in dispersion; and every dataset carries realistic measurement noise. This is still synthetic, and it does not stand in for real gravity, surface-wave, or magnetotelluric data. It asks a narrower question: does the joint test still work when the truth is out of model.

It does (Table 3). When the observed data come from the fertile prior, the fertile scenario admits the truth 99 per cent of the time and the rivals are rejected at 98 to 100 per cent.

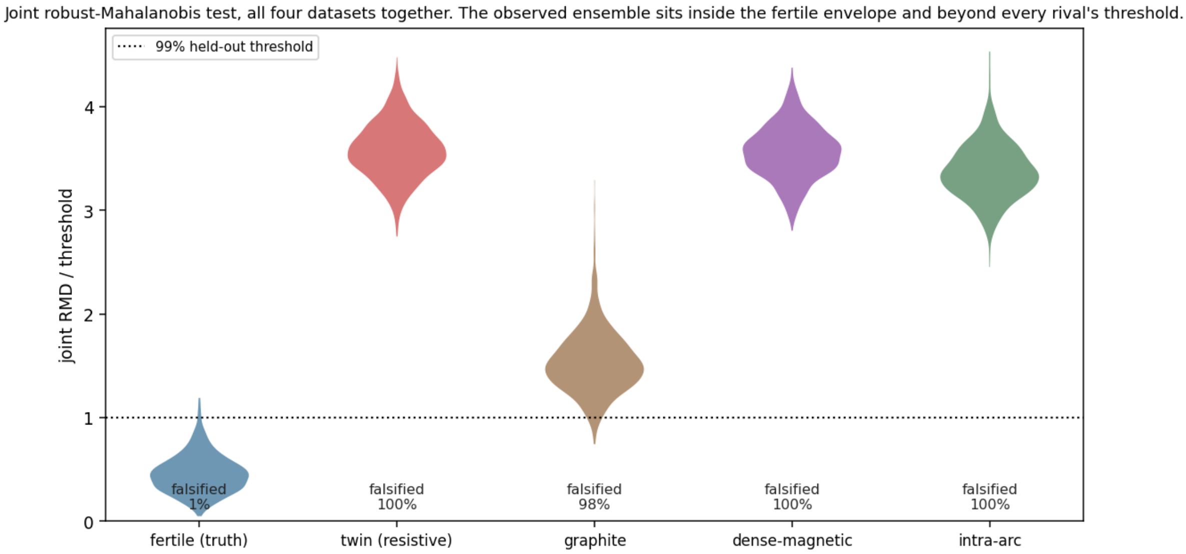

Figure 6: Joint robust-Mahalanobis test on all four datasets. The observed ensemble sits inside the fertile envelope at the nominal false-rejection rate and beyond every rival's threshold.

Table 3: Robustness of the joint discriminator when the observed data are out of model. Each row is a different way of generating the fertile truth. The fertile scenario should admit the truth (high is correct) and the four rivals should reject it (high is correct). The last column is the fraction of truths that are jointly classified correctly, fertile admitted and all rivals rejected.

Truth generation	fertile admits	twin rejects	graphite rejects	dense rejects	intra rejects	all correct
In model (fertile prior)	99%	100%	98%	100%	100%	97%
Out of model, params + noise	91%	100%	100%	100%	100%	91%
Out of model, + un-modelled structure	96%	100%	100%	100%	100%	96%

When the observed data are out of model, with independent parameters and noise, the fertile scenario still admits the truth 91 per cent of the time and every rival is rejected at 100 per cent. Adding the un-modelled secondary structure does not degrade this; the fertile admission rate is 96 per cent and the rivals are still rejected at 100 per cent. The joint discriminator is therefore a property of the tectonic tie between the datasets, not an artefact of testing against same-distribution synthetic truth.

4.3 Consistency with public data

As a first check against real data, we compare the modeled magnetic field of a georeferenced corridor model to a public satellite-airborne magnetic-anomaly grid (EMAG2v3; Meyer et al. 2017) over the corridor (Fig. 7). The observed field is mostly positive, with a mean of +39 nT and peaks near +277 nT. This matches the grounded expectation for an oxidised magnetite-series arc, the central Arabian anomaly. The local source model does not produce the long-wavelength regional field, so we remove that field before comparing. The observed short-wavelength residual and the modeled field then agree in sign balance, and the observed amplitude falls inside the modeled prior envelope. The model is smoother than the data. This is expected, because the real arc crust is more densely intruded than the idealised model, and the body positions are not

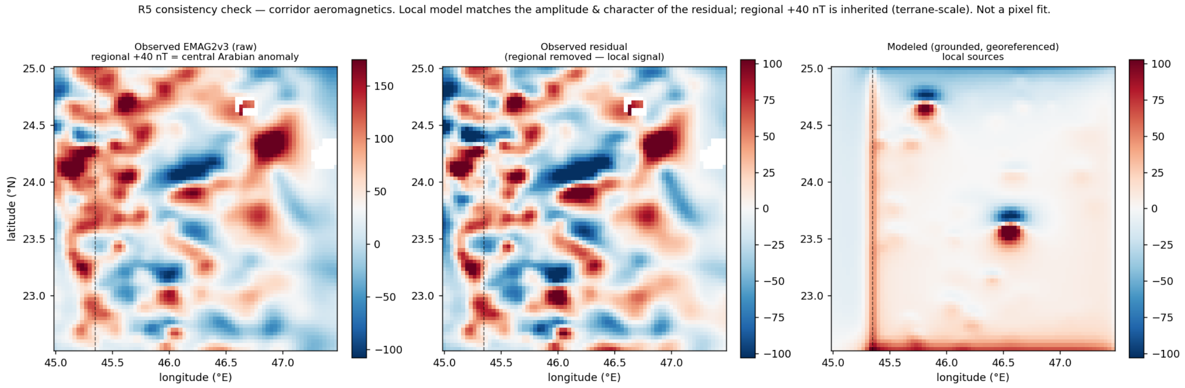

Figure 7: Modeled magnetics against public EMAG2v3 data over the corridor. Raw observed field (left), the short-wavelength residual after removing the regional field (middle), and the grounded model (right). The local model matches the amplitude and character of the residual. The raw +39 nT positive is the terrane-scale central Arabian anomaly. This is not a pixel fit.

constrained at this resolution. This is a regional check at about 3.7 km resolution. It is not a spatial fit. The high-resolution national grid would make a spatial fit possible.

The same presentation as the synthetic case then applies, with one real dataset. The magnetic-source priors are the arc, ophiolite, and intrusive rows of Table 2. Figure 8 shows three prior samples of the modelled field, processed identically to the data: the same regional removal and the same coverage mask. The comparison features are the residual standard deviation, the 98th-percentile amplitude, and the positive fraction. The residual mean is excluded, because the regional removal drives it to zero for model and data alike, so it carries no information. Figure 9 shows fifty modelled realisations against the observed values, and the individual and joint RMD. The outcome is a result, not a formality. Each feature is individually admissible: the observed standard deviation, amplitude, and positive fraction all fall inside the prior envelope, at 0.67, 0.31, and 0.41 of their thresholds. The joint test rejects the illustrative model, at 1.52 times the held-out 99 per cent threshold. The rejection quantifies the idealisation the qualitative comparison could only name: the observed residual is rougher than the modelled population (standard deviation 44 against an ensemble mean of 16 nT), because the real arc crust is more densely intruded and the body positions are unconstrained at this resolution. The joint test resolves what the individual tests cannot, on real data, which is the pattern the synthetic ablation predicts. The refinement it calls for is a denser intrusive-source population constrained by the high-resolution grid.

We test that refinement directly. Holding the susceptibilities at their grounded priors and varying only the intrusion density, we sweep the number of distributed magnetite bodies in the arc and recompute the joint statistic at each density. The result closes the loop (Fig. 10). At the illustrative density of about one body per 1000 km^2 the joint RMD is 1.52, the rejection above. Increasing the density moves the observed residual inside the model's envelope: the joint statistic falls monotonically and crosses the threshold at about three bodies per 1000 km^2, a modest intrusion density for a magmatic arc, reaching 0.3 at higher densities. Only one quantity is changed, the density, and its direction was fixed in advance by the rejection, so this is a confirmation rather than a fit. The crossing is a statement about the joint envelope, not a

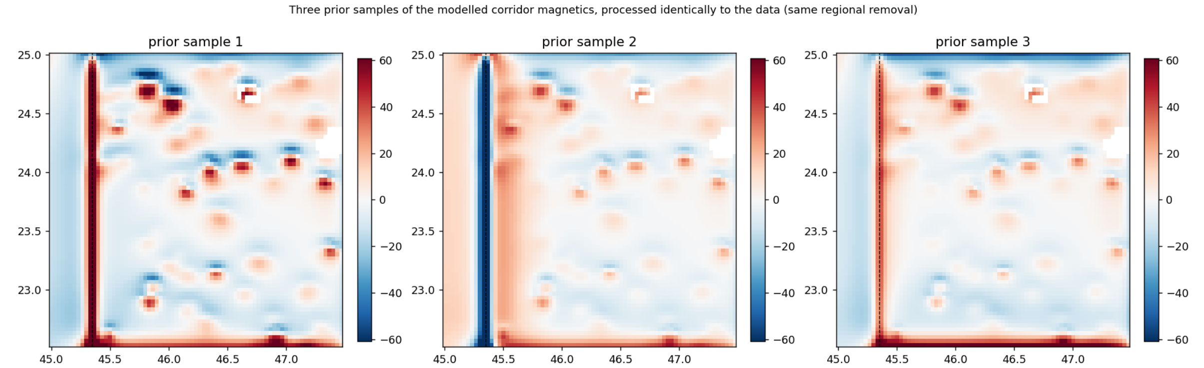

Figure 8: Real case, three prior samples of the modelled corridor magnetics, processed identically to the observed EMAG2v3 clip (same regional removal, same coverage mask). The susceptibilities and the suture remanence are drawn from the priors of Table 2; the body positions are illustrative.

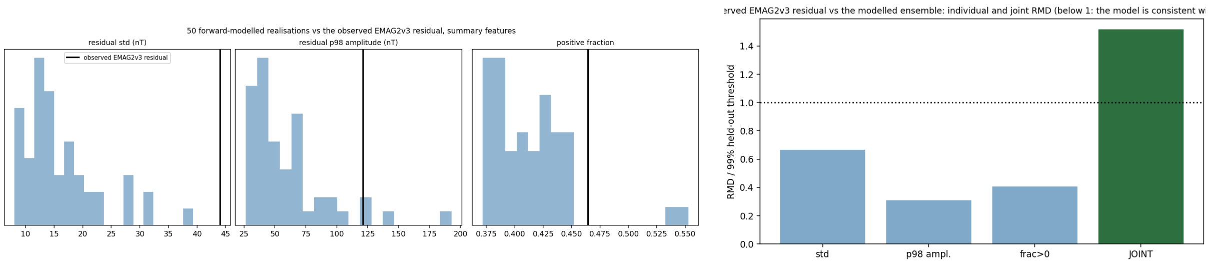

Figure 9: Real case, the test. Left: fifty forward-modelled realisations of the three summary features against the observed EMAG2v3 residual (black line). Right: the individual and joint RMD against the held-out 99 per cent threshold (dotted). Each feature is individually admissible; the joint test rejects the illustrative source population at 1.52 times the threshold, quantifying that the observed residual is rougher than the idealised model.

mean match: the modelled residual roughens toward the data as density rises but its mean standard deviation stays below the observed 44 nT (Fig. 10, right), and the observed vector sits at the rough edge of the widened envelope. The rejection named a denser intrusive population, implementing that population admits the data, and the falsification loop therefore closes on real magnetics. It remains one dataset and a regional check, not a spatial fit.

A second real dataset then tests the refined model from outside the channel that produced it. We extract the WGM2012 complete Bouguer anomaly (Bonvalot et al. 2012) over the same corridor, at the same 2-arcmin regional footing as the magnetic clip, and apply the identical treatment: the same regional removal, the same coverage mask, the same three summary features, and prior-predictive envelopes from the grounded density contrasts of Table 2, the east–west arc contrast, the wide sign-ambiguous ophiolite contrast of the serpentinisation ladder, and mafic intrusions. The source density is not tuned to this dataset; it is the value the magnetic rejection fixed in advance. The observed Bouguer residual, with a standard deviation of 8.5 mGal, a 98th-percentile amplitude of 19.5 mGal, and a positive fraction of 0.50, is individually admissible on every feature, at 0.18, 0.25, and 0.45 of the thresholds, and jointly admissible at 0.55 (Fig. 11). Gravity separates the two source densities less sharply than magnetics, both are admissible, at 0.80 for the sparse population and 0.55 for the refined one, which is expected because the intrusions contrast more strongly in susceptibility than in density. The direction agrees with the magnetic refinement: the denser population fits the gravity data better. Two real datasets now

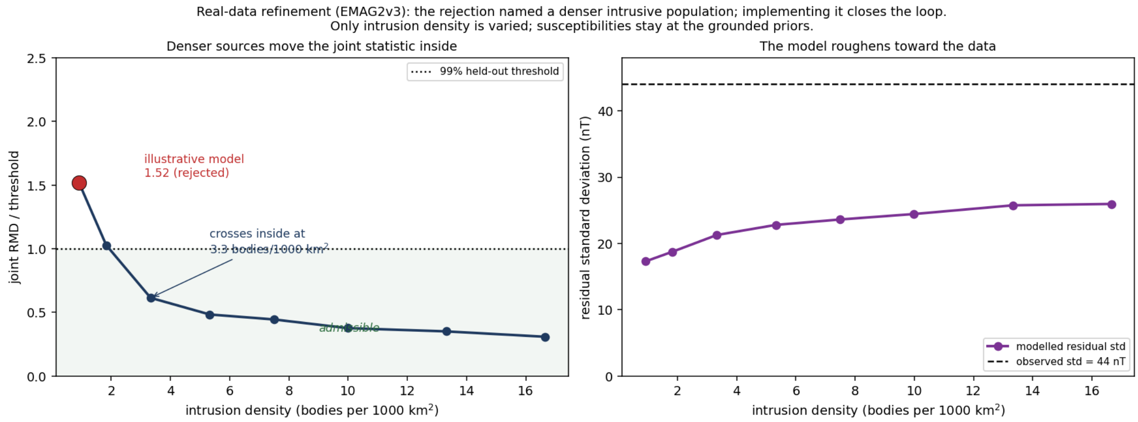

Figure 10: Closing the falsification loop on real data. Left: the joint RMD against the observed EMAG2v3 residual as a function of intrusion density. The illustrative model (red, one body per 1000 km^2) is rejected at 1.52; increasing density moves the joint statistic inside the 99 per cent threshold, crossing near three bodies per 1000 km^2. Right: the modelled residual standard deviation roughens toward the observed 44 nT as density rises. Only intrusion density is varied; susceptibilities are held at the grounded priors.

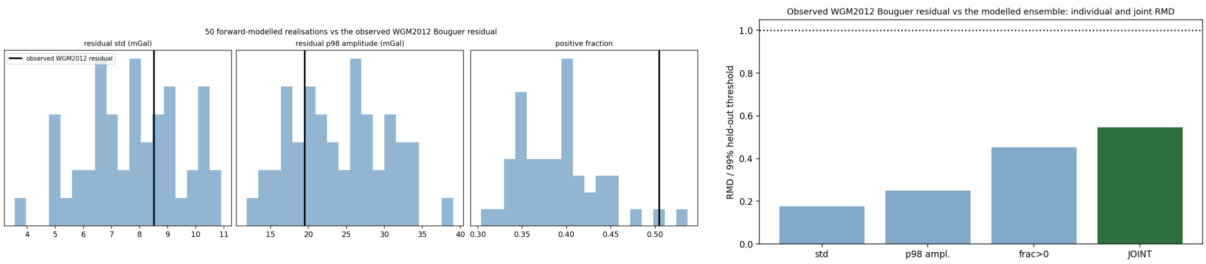

Figure 11: Real case, gravity. Left: fifty forward-modelled realisations of the three summary features against the observed WGM2012 Bouguer residual (black line), with the source density fixed in advance by the magnetic refinement and the density contrasts drawn from the grounded priors. Right: the individual and joint RMD against the held-out 99 per cent threshold (dotted). The observed residual is individually and jointly admissible.

constrain the model, one that rejected and recovered, and one that admits, and both prefer the same source population. The check remains regional; the corridor's own gravity signature, the serpentinite ambiguity of Section 2.6, is a target for the airborne survey, at a resolution this grid does not reach.

The velocity channel follows the same loop, with one honest downgrade: the public product is a published inversion, not measured dispersion. We extract the corridor-average shear-velocity column of the Middle East crustal model (Kaviani et al. 2020), run our verified dispersion forward on it, and treat the resulting Rayleigh phase-velocity curve as the observed data, so the comparison stays in data space but with an inversion in the loop, and every number below carries that caveat. Against the base column priors the observed curve is jointly rejected at 3.65 times the threshold (Fig. 12), and the rejection decomposes cleanly: the mid-crustal feature at 17 s is admissible, the 8 s feature rejects because the published model carries a shallow low-velocity layer, the eastern Phanerozoic section plus the inversion's weakly constrained near-surface, that the cover-free reference column lacks, and the 30 s feature rejects because the published deep structure is gradational and slower, with the shear velocity crossing 4.3 km s^{-1} only near

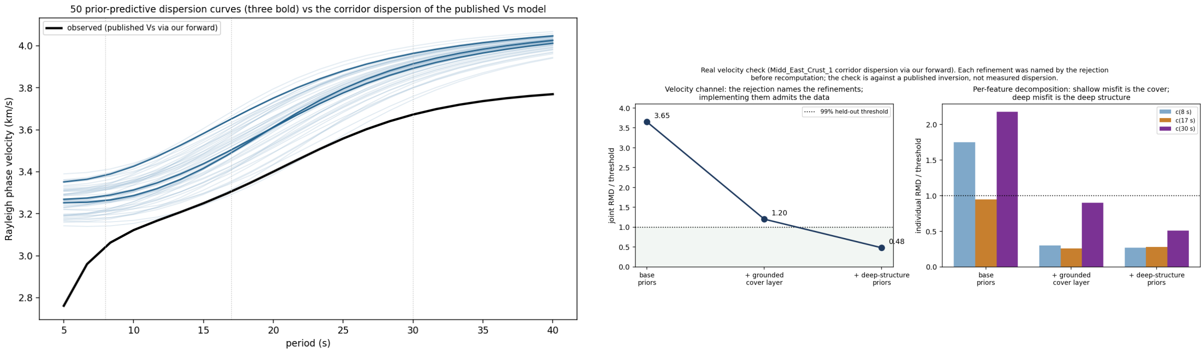

Figure 12: Real case, velocity. Left: fifty prior-predictive dispersion curves (three bold) against the corridor dispersion of the published shear-velocity model computed with our forward (black). Right: the refinement ladder. The base column is rejected at 3.65; the grounded cover layer moves the joint statistic to 1.20; the grounded deep-structure priors admit the data at 0.48. Each refinement was named by the rejection before recomputation; the check is against a published inversion, not measured dispersion.

43 km, than the sharp reference column. Both refinements were named by the rejection before recomputation. Adding a shallow layer drawn from the grounded cover unit moves the joint statistic to 1.20; widening the deep structure to its grounded ranges, a lower crust at N(4.00, 0.12), a mantle at N(4.50, 0.10), and a gradational Moho transition, admits the data at 0.48. Part of the deep misfit is plausibly the inversion's own smoothing rather than earth structure, and only measured dispersion can separate the two, which is the stated reason this check ranks below the magnetic and gravity ones.

The magnetotelluric channel is checked against measured data, the 122 impedance soundings of the public Harrat Rahat release (Bedrosian et al. 2024), so this check has no inversion in the loop. Its scope is bounded by geography and by a stated circularity. The sites lie several hundred kilometres from the corridor, so the check tests the background shield column, the host upper crust, the lower-crustal conductive band, and the mantle, and says nothing about the fertile corridor. And the conductive-band prior traces to the resistivity model built from these very data, so admission of the deep features is expected, and what the check validates is the compilation chain from prior through our forward to measured data; a rejection there would have indicated a broken link. The median determinant apparent-resistivity curve across the 122 stations, the rotation-invariant scalar given the documented lower-crustal anisotropy, is admitted on the deep features at 0.41 and 0.24 of their thresholds. The short-period feature rejects at 2.09, and the reason is documented in the survey's own reports: the stations sit on Harrat Rahat lavas, a sediment-filled graben, and sabkha, so the measured 1 s response is local surficial geology that the exposed-shield background column never claimed to represent. A surficial layer with the survey's own site description, up to 3 km thick, wide in resistivity because the sites span resistive lava and conductive sabkha, admits the data at 0.38 (Fig. 13). That layer is site geology at Harrat Rahat; it changes nothing in the corridor prior. The corridor's own magnetotelluric response remains unmeasured, and it is the decisive acquisition.

Across the four channels a pattern stands out. Every real dataset that rejected did so for a specific, nameable, geologically sensible reason, the intrusive density in magnetics, the cover and the deep structure in dispersion, the surficial site geology in magnetotellurics, and in every case

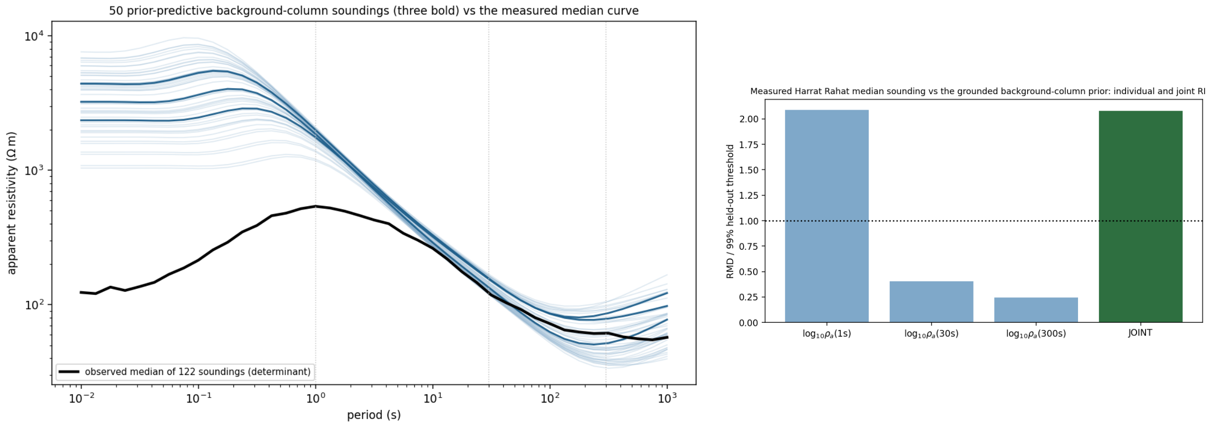

Figure 13: Real case, magnetotellurics. Left: fifty prior-predictive background-column soundings (three bold) against the median determinant apparent-resistivity curve of the 122 measured Harrat Rahat soundings (black). Right: the individual and joint RMD of the base background column. The deep features, the ones grounded in the model built from these data, are admitted; the 1 s feature rejects for the documented local surficial geology, and a site-geology surficial layer admits the data at 0.38. The sites are several hundred kilometres from the corridor: this validates the compilation chain, and the corridor transect remains the decisive acquisition.

implementing the named refinement admitted the data. The falsification loop has now run on real data four times.

5 Discussion

The method is a controlled path from a geologist's tectonic history to falsifiable multiphysics prediction. Each link is grounded in a public source, checked against a limit, and calibrated. The main scientific result is that the fertile-corridor discriminator is joint, and that MT is required but not sufficient. This result holds under an honest treatment of the weakest input, the marginalised remanence direction, and it survives a calibrated test. The approach also avoids a failure mode of deterministic inversion. The geological prior here is explicit and provenance-tagged. It cannot quietly dominate a weakly-informative dataset the way a smoothing prior can. A narrow fertile corridor enters as a hypothesis to test. A minimum-structure inversion would instead smooth such a body away: a concrete demonstration on the corridor's own magnetotelluric response, in which the narrow conductor is smeared into a broad low indistinguishable from a barren graphitic zone, is in Appendix C (Fig. 20). The graphite confounder is central to the result. A single dataset, MT, is ambiguous, because interconnected graphite reproduces the fertile conductance. The tie to the other datasets and to the tectonic history removes the ambiguity, because the history predicts how the four datasets should behave together. This is why the joint reading separates fertile from barren where one dataset cannot.

The same falsification also reports which part of the tectonic history carries the result. Two readings of the compiled prior give this (Fig. 14). The first is a drop-one sensitivity of the discrimination. We remove each clause's dataset from the joint test and measure how the power to reject the barren rivals changes. Removing the fertile-corridor clause, which the magnetotelluric conductance carries, collapses the joint falsification from 97 to 1 per cent, because the resistive twin then survives. Removing the serpentinised-suture clause, carried by gravity, costs 37 points, because gravity is what rejects the graphite rival. Removing the metasomatism clause, carried by dispersion, costs 12. Removing the magnetite-arc and Najd-remanence clause, carried by magnetics, changes nothing and slightly improves the result, because the marginalised remanence direction adds spread to the magnetic feature without adding separation. The second reading is the information the data gained about each clause. We condition the surviving prior on one observation and compare each clause parameter's surviving width to its prior width. The corridor conductivity, the suture density, and the metasomatic velocity each narrow by about half. The magnetite-arc susceptibility and the Najd remanence direction do not narrow, because one observation of the magnetic field cannot separate an induced from a remanent contribution, and no dataset constrains a marginalised direction.

Read together, the two axes annotate the history (Fig. 14). The corridor-conductivity clause is load-bearing. It is both decisive and informed, and it is the sentence to state most carefully. The suture-density and metasomatism clauses are informed and support the discrimination without carrying it. The strike-slip remanence clause is untested. The data neither constrain it nor need it, and as written it is a liability, because it makes magnetics ambiguous. This is a quantitative form of the honest treatment the method already applies to the remanence direction, and it is an output the geologist can act on. An untested clause is a candidate for revision, because the narrative asserts something the available data cannot see, or it is a target for acquisition, because a measurement that would test it, here a palaeomagnetic constraint on the remanence, would change what the joint reading can do. The method returns this reading as an updated history: each clause tagged by how much it carried the result and how much the data informed it, which tells the geologist where to sharpen the narrative and where to point the next survey. The same drop-one procedure applies to the geometric clauses through the generator, so the dip, the offset, and the corridor extent can be ranked the same way.

The claims are bounded, and the boundary between real and synthetic evidence should be stated plainly. All four datasets are now checked against real observations, each within a stated scope. Magnetics, against the public EMAG2v3 grid, closes the loop: the over-smooth model is rejected and a denser intrusive population admits the data. Gravity, against the public WGM2012 Bouguer grid, admits the model at the source density magnetics fixed. Dispersion, against the corridor column of a published shear-velocity inversion pushed through our forward, closes its loop in two grounded steps, with the inversion-in-the-loop caveat stated. Magnetotellurics, against the 122 measured Harrat Rahat soundings, validates the background compilation chain, with the geographic and circularity caveats stated, and does not touch the corridor. The synthetic demonstration is more than a self-consistency check, because the discriminator survives out-of-model truth (Table 3), but it is not corridor-scale real-data validation, and the corridor magnetotelluric response, on which the discriminator most depends, remains unmeasured. Closing each gap needs a specific public dataset now and the targeted survey later. For the density channel the check is done: the WGM2012 complete Bouguer anomaly (Bonvalot et al. 2012) over the corridor admits the model individually and jointly at the source density the magnetic rejection fixed (Section 4.3), at the same 2-arcmin regional footing as the magnetic check. For the velocity channel the check is done against the Middle East crustal model (Kaviani et al.

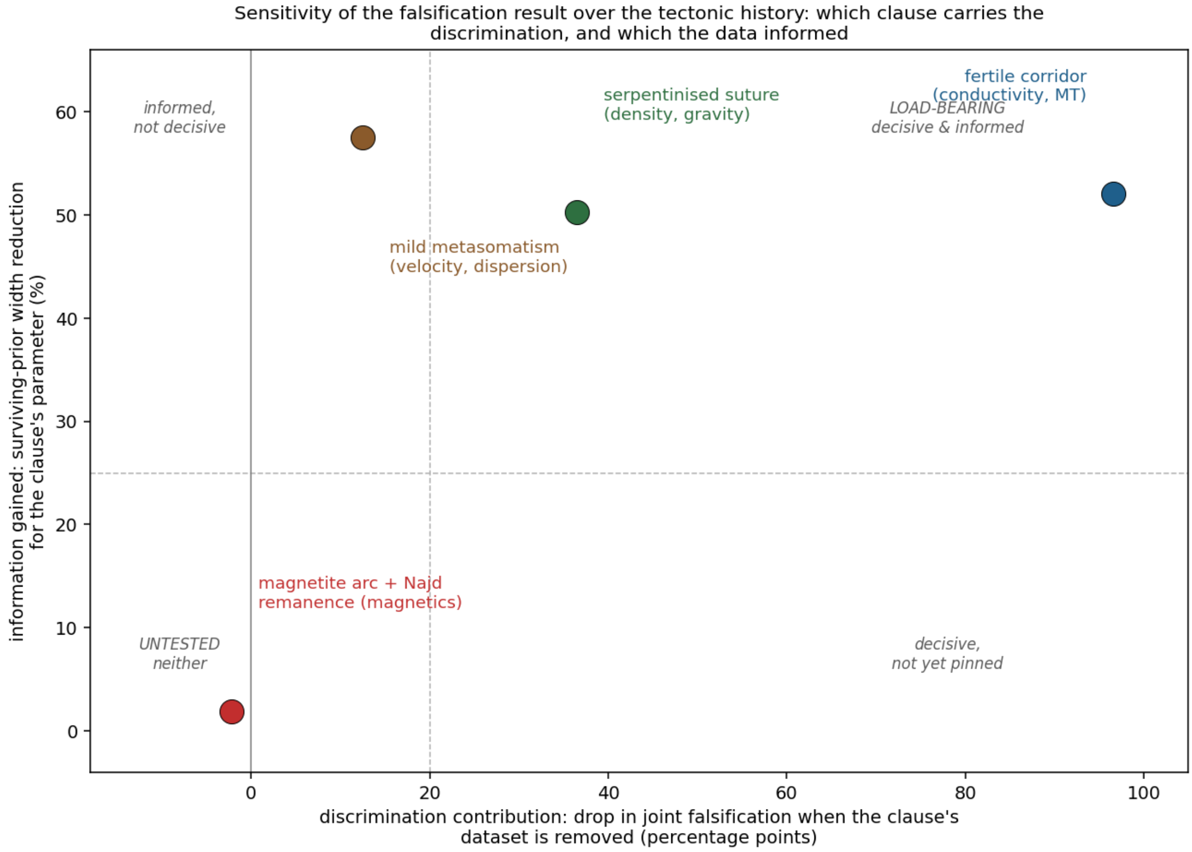

Figure 14: Sensitivity of the falsification result over the tectonic history. Horizontal: the drop in joint falsification of the barren rivals when a clause's dataset is removed, so how much that clause carries the discrimination. Vertical: the reduction in the clause parameter's surviving-prior width after conditioning on one observation, so how much the data informed it. The corridor-conductivity clause is load-bearing; the suture-density and metasomatism clauses are informed and supporting; the magnetite-arc and Najd-remanence clause is untested, and as written it makes magnetics ambiguous.

2020), with measured Shield dispersion (Civilini et al. 2023) the stronger future check. For the conductivity channel the check is done against the measured Harrat Rahat impedances (Bedrosian et al. 2024), several hundred kilometres from the corridor; the corridor transect is the acquisition item, and it is the measurement the discriminator most needs. The other boundaries stand as before: the forward models are coarse and the magnetotelluric solver is TE-mode, so the graphite confounder is not tested against the TM-mode and anisotropic response that would most sharply separate it; the body positions in the georeferenced comparison are illustrative; and the compiler is run on one ratified history, with its full fidelity study in the companion paper (Caers in prep.). Together these define the work needed to turn the prototype into a tool.

That work is the acquisition, and the sensitivity above points to it. The prior that survives falsification is the basis for planning what to measure next. A rejected prior is discarded; the surviving prior is a calibrated statement of what is still uncertain, with each uncertain quantity carrying the distribution the tectonic history licensed. Designing a survey against a rejected prior would waste effort chasing a structure the data already rule out. Designing it against the surviving prior targets the quantities that still separate the live hypotheses. This inverts the usual order. The screening step decides which structures remain possible, and only then does acquisition planning begin, on the reduced set.

The design is expert-driven, not automatic. The geologist specifies the variable whose uncertainty they want reduced, because that choice encodes the geological decision the survey must serve, and the method then reports how informative each measurement would be about that variable under the surviving prior. The suture dip at depth is one such example. It is a draft prior in Table 1, unconstrained by public data, and it controls whether the corridor is a steep suture-hosted conduit or a shallow intra-arc feature, so reducing its uncertainty changes the prospectivity call. A geologist who nominates the dip would be shown which of a reflection line, a denser magnetotelluric transect, or receiver-function coverage most tightens its posterior, given how the tectonic history ties the dip to the observables. The three-dimensional velocity structure over the corridor, the deep corridor conductivity, and the cover thickness are the other draft quantities a geologist might nominate. A targeted airborne-gravity, ambient-noise, and magnetotelluric survey would measure them, and because the surviving prior predicts how they behave together, the method ranks the candidate surveys by the uncertainty reduction each buys on the nominated variable.

6 Conclusions

We built and tested a country-scale method. A geologist's tectonic history is compiled, by a language model used as a constraint extractor, into a falsifiable, provenance-grounded multiphysics prior. Candidate geological scenarios are then judged by calibrated falsification of their joint gravity, magnetic, seismic, and magnetotelluric behaviour. On the Al Amar–Halaban and Najd system of the Arabian Shield, the method shows that a fertile deep corridor changes density by a small amount, lowers velocity by a few per cent, and raises deep conductance about sixfold. No single dataset separates this corridor from barren rivals built to mimic it. The four datasets read together do separate it. MT is required, and because of the graphite confounder it is not sufficient on its own. Every prior is tied to public data, every forward model is benchmarked, the falsification test is calibrated, and the same test applied to public aeromagnetic data rejects an over-smooth source model, after which the denser intrusive population the rejection names moves the data back inside the envelope and closes the loop on real magnetics; the same loop then runs on public gravity, a published shear-velocity model, and measured magnetotelluric soundings, each within its stated scope, and every rejection is closed by a grounded correction the rejection itself named. The quantities the method leaves unconstrained are its survey recommendation, and because the prior that survives falsification is a calibrated statement of what is still uncertain, it is the basis for designing that survey: the geologist nominates the variable whose uncertainty is to be reduced, the suture dip being one example, and the method ranks the candidate measurements by how much each tightens it.

Data and code availability

All priors are tied to public sources listed in the grounding documentation. The compiler schema, the lithospheric generator, the three forward models with their benchmarks, the petrophysical prior module, and the falsification and calibration scripts are self-contained and will be released. Public datasets used: EMAG2v3 (Meyer et al. 2017); USGS Open-File Report 2023-1042 (Blanchette et al. 2023); and the magnetotelluric release of Bedrosian et al. (2019).

References

Al-Husseini, M. & Stewart, I.C.F., 2026. Aeromagnetic mapping and geodynamic reconstruction of the Ediacaran Najd fault system in the Arabian Shield, *Gondwana Res.*, **153**, 38–59, doi:10.1016/j.gr.2025.11.019.

Bedrosian, P.A., Peacock, J.R., Dhary, M., Sharif, A., Feucht, D.W. & Zahran, H., 2019. Crustal magmatism and anisotropy beneath the Arabian Shield: a cautionary tale, *J. geophys. Res. Solid Earth*, **124**, 10153–10179, doi:10.1029/2019JB017903.

Bedrosian, P.A., Peacock, J.R. & Feucht, D.W., 2024. Magnetotelluric data from northern Harrat Rahat, Saudi Arabia, 2016, *U.S. Geological Survey data release*, doi:10.5066/P99H8HJ7.

Blanchette, A.R., Klemperer, S.L. & Mooney, W.D., 2023. Crustal thickness and the Vp/Vs ratio within the Arabia Plate from P-wave receiver functions at 154 broadband seismic stations, *U.S. Geol. Surv. Open-File Rep.* 2023-1042, doi:10.3133/ofr20231042.

Bonvalot, S., Balmino, G., Briais, A., Kuhn, M., Peyrefitte, A., Vales, N., Biancale, R., Gabalda, G., Reinquin, F. & Sarrailh, M., 2012. *World Gravity Map*, Commission for the Geological Map of the World, Eds. BGI-CGMW-CNES-IRD, Paris, doi:10.18168/bgi.23.

Clark, D.A., 1997. Magnetic petrophysics and magnetic petrology: aids to geological interpretation of magnetic surveys, *AGSO J. Aust. Geol. Geophys.*, **17**(2), 83–103.

Caers, J., in preparation. A language model as a compiler: from tectonic narrative to a falsifiable prior, companion paper.

Civilini, F., Mooney, W.D., Savage, M.K. & Townend, J., 2023. Ambient seismic noise tomography of the Kingdom of Saudi Arabia, chap. N of Sisson, T.W., Calvert, A.T. & Mooney, W.D., eds, *Active Volcanism on the Arabian Shield*, U.S. Geological Survey Professional Paper 1862, 57 pp., doi:10.3133/pp1862N.

Constable, S.C., Parker, R.L. & Constable, C.G., 1987. Occam's inversion: a practical algorithm for generating smooth models from electromagnetic sounding data, *Geophysics*, **52**(3), 289–300, doi:10.1190/1.1442303.

Dagdelen, J., Dunn, A., Lee, S., Walker, N., Rosen, A.S., Ceder, G., Persson, K.A. & Jain, A., 2024. Structured information extraction from scientific text with large language models, *Nat. Commun.*, **15**, 1418, doi:10.1038/s41467-024-45563-x.

deGroot-Hedlin, C. & Constable, S., 1990. Occam's inversion to generate smooth, two-dimensional models from magnetotelluric data, *Geophysics*, **55**, 1613–1624.

Deng, C., Zhang, T., He, Z., Chen, Q., Shi, Y., Xu, Y., Fu, L., Zhang, W., Wang, X., Zhou, C., Lin, Z. & He, J., 2024. K2: a foundation language model for geoscience knowledge understanding and utilization, in *Proc. 17th ACM Int. Conf. Web Search and Data Mining (WSDM '24)*, pp. 161–170, doi:10.1145/3616855.3635772.

Doebrich, J.L., Al-Jehani, A.M., Siddiqui, A.A., Hayes, T.S., Wooden, J.L. & Johnson, P.R., 2007. Geology and metallogeny of the Ar Rayn terrane, eastern Arabian shield, *Precambrian Res.*, **158**, 17–50, doi:10.1016/j.precamres.2007.04.003.

Gallardo, L.A. & Meju, M.A., 2003. Characterization of heterogeneous near-surface materials by joint 2-D inversion of dc resistivity and seismic data, *Geophys. Res. Lett.*, **30**(13), 1658, doi:10.1029/2003GL017370.

Gettings, M.E., Blank, H.R., Mooney, W.D. & Healey, J.H., 1986. Crustal structure of southwestern Saudi Arabia, *J. geophys. Res.*, **91**(B6), 6491–6512.

Herrmann, R.B., 2013. Computer Programs in Seismology: an evolving tool for instruction and research, *Seismol. Res. Lett.*, **84**, 1081–1088.

Hunt, C.P., Moskowitz, B.M. & Banerjee, S.K., 1995. Magnetic properties of rocks and minerals, in *Rock Physics and Phase Relations: A Handbook of Physical Constants*, AGU Ref. Shelf 3, pp. 189–204.

Jessell, M., Aillères, L., de Kemp, E., Lindsay, M., Wellmann, F., Hillier, M., Laurent, G., Carmichael, T. & Martin, R., 2014. Next generation three-dimensional geologic modeling and inversion, *Soc. Econ. Geol. Spec. Publ.*, **18**, 261–272.

Jessell, M.W. & Valenta, R.K., 1996. Structural geophysics: integrated structural and geophysical modelling, in *Structural Geology and Personal Computers*, Computer Methods in the Geosciences 15, pp. 303–324, Pergamon, doi:10.1016/S1874-561X(96)80027-7.

Kaviani, A., Paul, A., Moradi, A., Mai, P.M., Pilia, S., Boschi, L., Rümpker, G., Lu, Y., Tang, Z. & Sandvol, E., 2020. Crustal and uppermost mantle shear wave velocity structure beneath the Middle East from surface wave tomography, *Geophys. J. Int.*, **221**, 1349–1365, doi:10.1093/gji/ggaa075.

Li, Y. & Oldenburg, D.W., 1996. 3-D inversion of magnetic data, *Geophysics*, **61**(2), 394–408, doi:10.1190/1.1443968.

Li, Y. & Oldenburg, D.W., 1998. 3-D inversion of gravity data, *Geophysics*, **63**(1), 109–119, doi:10.1190/1.1444302.

Lin, Z., Deng, C., Zhou, L., Zhang, T., Xu, Y., Xu, Y., He, Z., Shi, Y., Dai, B., Song, Y., Zeng, B., Chen, Q., Shi, T., Huang, T., Xu, Y., Wang, S., Fu, L., Zhang, W., He, J., Ma, C., Zhu, Y., Wang, X. & Zhou, C., 2024. GeoGalactica: a scientific large language model in geoscience, *arXiv preprint* arXiv:2401.00434.

Linde, N., Renard, P., Mukerji, T. & Caers, J., 2015. Geological realism in hydrogeological and geophysical inverse modeling: a review, *Adv. Water Resour.*, **86**, 86–101, doi:10.1016/j.advwatres.2015.09.019.

McCuaig, T.C. & Hronsky, J.M.A., 2014. The mineral system concept: the key to exploration targeting, *Soc. Econ. Geol. Spec. Publ.*, **18**, 153–175.

Meyer, B., Saltus, R. & Chulliat, A., 2017. EMAG2v3: Earth Magnetic Anomaly Grid (2-arc-minute resolution), NOAA Natl Cent. Environ. Inf., doi:10.7289/V5H70CVX.

Mooney, W.D., Gettings, M.E., Blank, H.R. & Healy, J.H., 1985. Saudi Arabian seismic deep-refraction profile: a traveltime interpretation of crustal and upper mantle structure, *Tectonophysics*, **111**, 173–246.

Moorkamp, M., Heincke, B., Jegen, M., Roberts, A.W. & Hobbs, R.W., 2011. A framework for 3-D joint inversion of MT, gravity and seismic refraction data, *Geophys. J. Int.*, **184**(1), 477–493, doi:10.1111/j.1365-246X.2010.04856.x.

Mosegaard, K. & Tarantola, A., 1995. Monte Carlo sampling of solutions to inverse problems, *J. geophys. Res.*, **100**(B7), 12431–12447.

Scheidt, C., Li, L. & Caers, J., 2018. *Quantifying Uncertainty in Subsurface Systems*, Geophys. Monogr. Ser. 236, John Wiley & Sons, doi:10.1002/9781119325888.

Tarantola, A., 2006. Popper, Bayes and the inverse problem, *Nature Phys.*, **2**, 492–494, doi:10.1038/nphys375.

Wei, X., Yin, Z., Bonner, W. & Caers, J., 2026. Falsification of geological hypotheses using drillholes and geophysics, *Surv. Geophys.*, **47**, 289–315, doi:10.1007/s10712-026-09936-9.

Wellmann, F. & Caumon, G., 2018. 3-D structural geological models: concepts, methods, and uncertainties, *Adv. Geophys.*, **59**, 1–121, doi:10.1016/bs.agph.2018.09.001.

Zhdanov, M.S., Varentsov, I.M., Weaver, J.T., Golubev, N.G. & Krylov, V.A., 1997. Methods for modelling electromagnetic fields: results from COMMEMI, *J. appl. Geophys.*, **37**(3–4), 133–271, doi:10.1016/S0926-9851(97)00013-X.

Zhu, J., Wang, Y., Tong, W., Li, S., Wang, M. & Wang, C., 2026. Gold deposit ontology guides a large language model to transform text into knowledge graphs for gold deposits, *Minerals*, **16**(1), 50, doi:10.3390/min16010050.

A Verification of the forward models

Gravity and magnetics use exact rectangular-prism summation: Nagy gravity, and Poisson-relation magnetics with induced and optional remanent magnetisation. The code reproduces the point-mass and dipole limits to 3×10^{-8} and 10^{-6} relative error and satisfies the Laplace

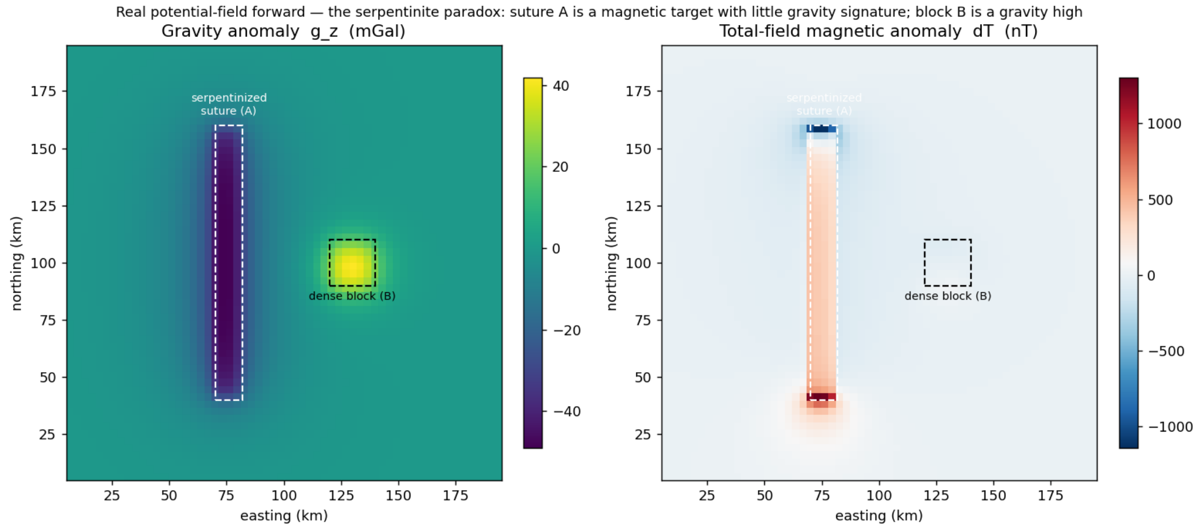

Figure 15: Gravity and magnetic response of a serpentinised suture and a dense block, from the prism forward with grounded priors. The suture reads as a magnetic high and a gravity low, because serpentinisation lowers density and raises susceptibility.

identity to machine precision. On a serpentinised suture the density falls and the susceptibility rises, so the body reads as a magnetic high with a weak or negative gravity signature (Fig. 15).

Surface-wave dispersion uses propagator-matrix methods (via disba, checked against Herrmann's surf96), which reproduces the half-space Rayleigh limit for a Poisson solid ($0.9194\,V_s$) exactly; a 5 per cent rise in V_s raises phase velocity by 4.3 per cent. A 6 per cent deep velocity reduction in the corridor shifts phase velocity by about 3 per cent near 17 s (Fig. 16). Many processes lower velocity, so this signal is not unique, and dispersion alone is weak.

Magnetotellurics uses an exact one-dimensional recursion and a two-dimensional transverse-electric finite-difference solver. The two-dimensional solver reproduces the one-dimensional limit to 0.02 per cent in apparent resistivity and 0.57° in phase, with second-order convergence, and it reproduces the COMMEMI 2D-1 community benchmark: on the standard 0.5 Ω m block in a 100 Ω m half-space at 10 Hz, the TE apparent resistivity at all five standard surface sites falls within the published inter-code spread and converges to the reference as the grid is refined (Zhdanov et al. 1997, Fig. 17). Two dimensions are needed because the corridor is a laterally confined conductor; a one-dimensional-per-column treatment drops the lateral current channelling that gives the corridor its signature. A confined fertile corridor produces a localised deep apparent-resistivity low, an 85 per cent drop directly over the corridor near 100 to 200 s (Fig. 18), and raises deep conductance from about 500 to about 3100 S. The solver is TE-mode; TM and anisotropic modelling, which bear on the graphite confounder, are the next step.

B Calibration of the falsification test

The falsification test is useful only if it rarely rejects the true scenario. We measure the false-rejection rate against ensemble size, feature dimensionality, and threshold choice (Fig. 19). The chi-square threshold is biased even for large ensembles. It sits near twice the nominal rate and does not converge, because the features are non-Gaussian. The empirical percentile threshold is

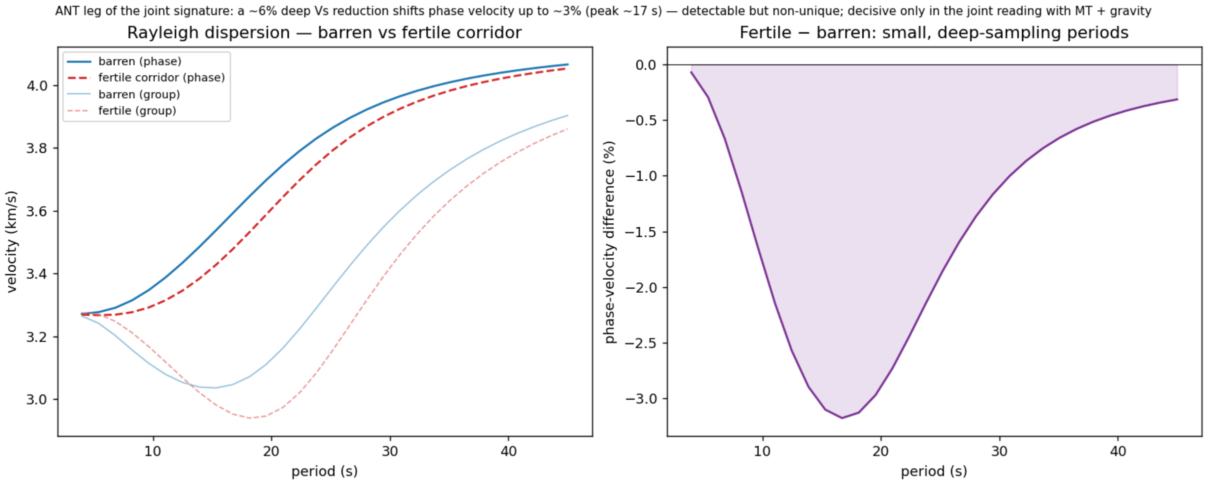

Figure 16: Rayleigh dispersion for a barren column and a fertile-corridor column. A 6 per cent deep velocity reduction shifts phase velocity by up to about 3 per cent near 17 s. The signal is detectable but not unique.

distribution-free and converges to the nominal rate, and a held-out empirical threshold is best. Ensemble size matters. Below about twenty draws per dimension the covariance is unstable and the false-rejection rate rises to between 5 and 17 per cent. We adopt the held-out empirical threshold and require at least about fifty draws per dimension. The ablation uses a thousand draws per dimension.

C Construction detail and demonstrations

The five tectonic primitives of the Al Amar history, each carried from the geologist's statement through the compiled prior to its forward signature, are shown in Fig. 21. The scenario feature priors of the falsification ablation are in Table 4. The smoothing-inversion demonstration referenced in the Discussion follows. Fig. 20 makes this concrete on the corridor itself. We take a narrow, high-contrast conductor at 20 km depth, compute its magnetotelluric response, add noise, and run a minimum-structure inversion. With informative data the inversion recovers a conductor broadened from 2 to about 8 km and weakened from 5 to about 9 Ω m, still near the right depth. With weakly-informative data the smoothing prior takes over. The same corridor is recovered as a broad, weak conductor spread over about 20 km and displaced 6 km deeper, with a peak resistivity five times too high. Both models fit their data. A geologist reading the second model sees a diffuse deep conductor. The narrow corridor is gone, and the smoothed image cannot be told from a broad barren graphitic zone.

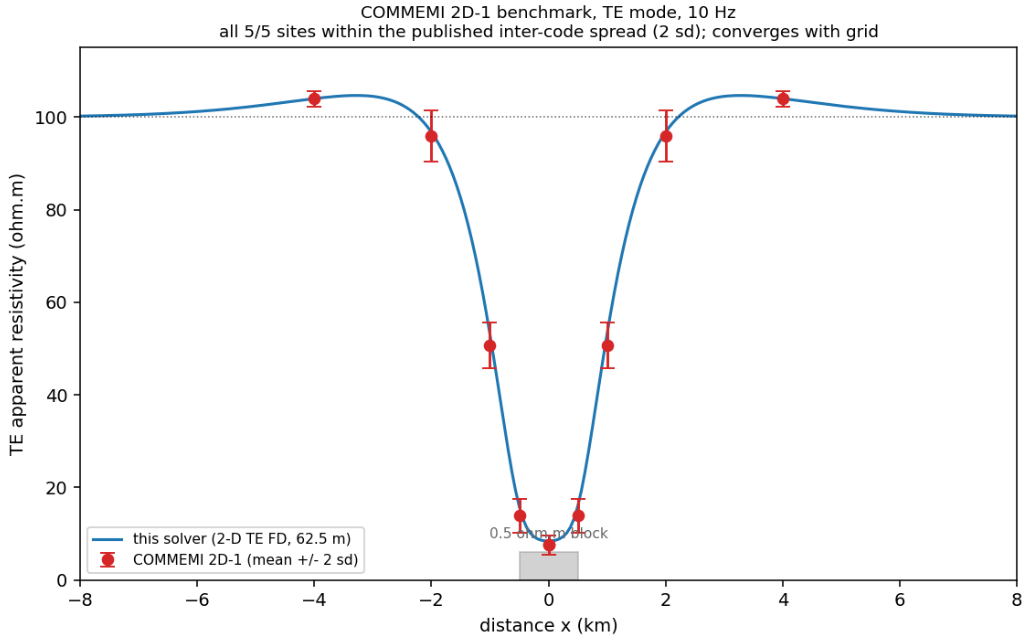

Figure 17: COMMEMI 2D-1 benchmark, TE mode at 10 Hz. The solver (line) against the published inter-code reference (Zhdanov et al. 1997) at the five standard sites (points, mean ±2 standard deviations). All five sites fall within the published spread, and the solution converges with grid.

Table 4: Scenario feature priors for the falsification ablation. Each entry is a normal prior N(μ, σ); susceptibility is clipped positive; the corridor resistivity prior is normal in $\log_{10}$. The fertile column is grounded (Table 2; Bedrosian et al. 2019); each rival copies the fertile prior on the feature it mimics (bold) and takes a barren prior elsewhere. All scenarios share the remanence prior, a Koenigsberger ratio $Q \sim$ U(0.5, 5) with a marginalised direction.

Random variable	Unit	Fertile	Twin	Graphite	Dense	Intra-arc
$\Delta\rho$: density contrast	$\mathrm{kg\,m^{-3}}$	N(−30, 40)	**N(−30, 40)**	N(180, 50)	**N(−30, 40)**	N(150, 50)
χ: susceptibility	SI	N(.040, .012)	**N(.040, .012)**	N(.015, .005)	**N(.040, .012)**	N(.015, .005)
ΔV_s: velocity change	%	N(−5, 1.5)	**N(−5, 1.5)**	N(0, 1.5)	N(0, 1.5)	**N(−5, 1.5)**
$\log_{10}\rho_e$: resistivity	$\log_{10}\Omega\,\mathrm{m}$	N(0.70, .15)	N(2.70, .15)	**N(0.70, .15)**	N(2.70, .15)	N(2.60, .15)

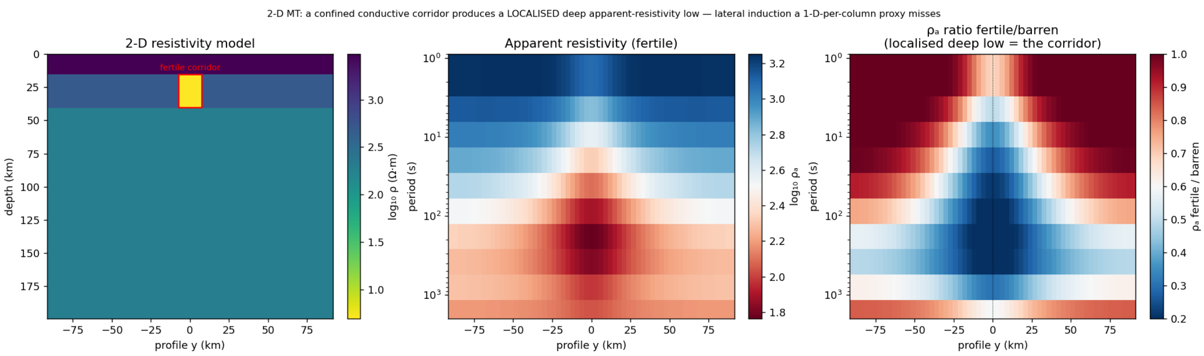

Figure 18: Two-dimensional TE magnetotelluric response of a laterally confined fertile corridor. The resistivity model (left), the apparent-resistivity pseudosection (middle), and the ratio to the barren case (right). The corridor produces a localised deep low that a one-dimensional-per-column treatment cannot represent.

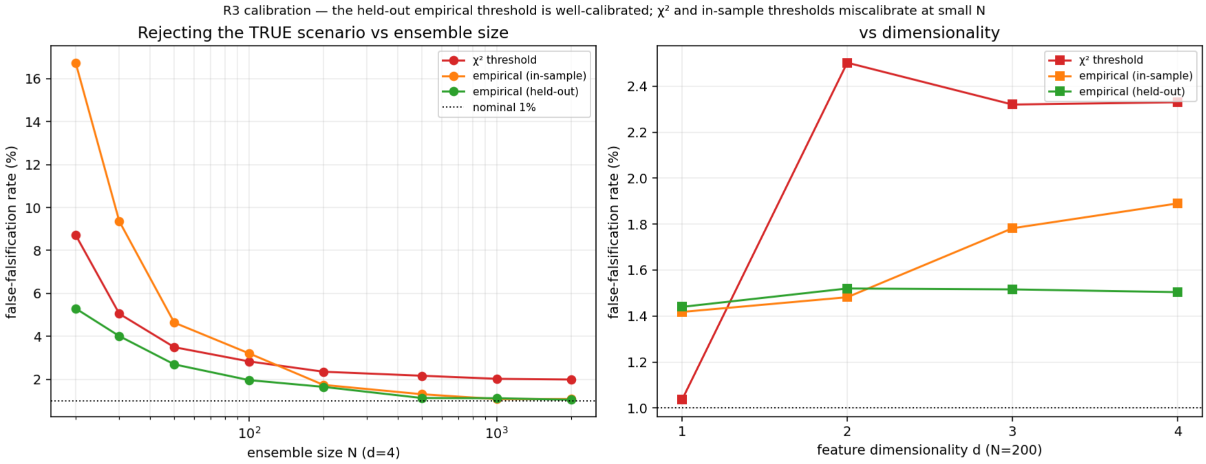

Figure 19: False-rejection rate of the true scenario against ensemble size (left) and feature dimensionality (right). The chi-square threshold sits near twice the nominal 1 per cent and does not converge. The empirical thresholds converge to nominal; the held-out version is best. Small ensembles are unreliable.

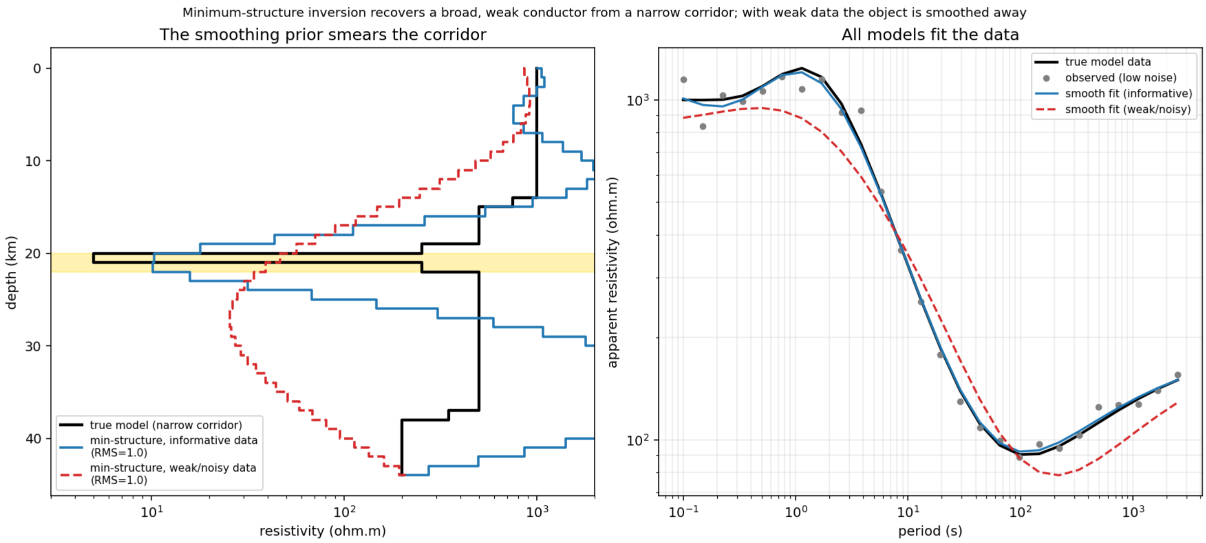

Figure 20: Minimum-structure inversion of the corridor's magnetotelluric response. The true model is a narrow conductor at 20 km (left, black). With informative data the smooth inversion broadens and weakens it. With weak data the conductor is smeared into a broad, mislocated low. Both fit their data (right).

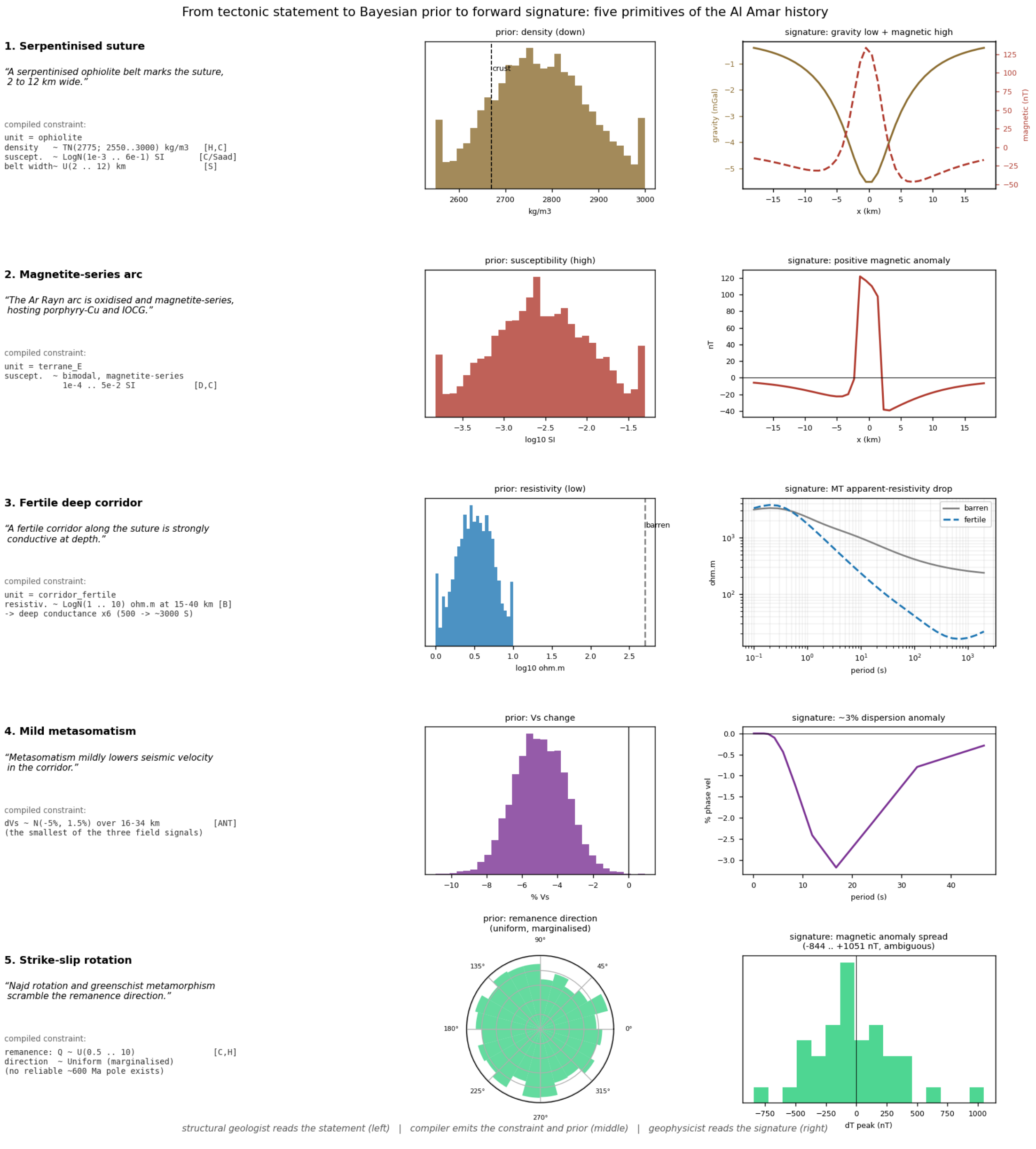

Figure 21: Five tectonic primitives of the Al Amar history. Each row runs from the geologist's statement (left), through the compiled constraint and prior (middle), to the forward signature computed by the real forwards (right). The serpentinised suture gives a density-down, susceptibility-up prior and a gravity-low, magnetic-high signature. The magnetite-series arc gives a positive magnetic anomaly. The fertile corridor gives a low-resistivity prior and a magnetotelluric apparent-resistivity drop. Mild metasomatism gives a small velocity reduction and a weak dispersion anomaly. Strike-slip rotation gives a marginalised remanence direction and a magnetic anomaly that is wide and ambiguous.